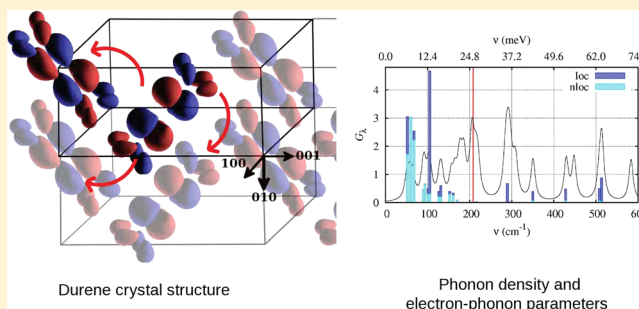


Charge Transport Properties of Durene Crystals from First-Principles

Carlo Motta* and Stefano Sanvito

School of Physics, AMBER and CRANN Institute, Trinity College, College Green, Dublin 2, Ireland

ABSTRACT: We establish a rigorous computational scheme for constructing an effective Hamiltonian to be used for the determination of the charge carrier mobility of pure organic crystals at finite temperature, which accounts for van der Waals interactions, and it includes vibrational contributions from the entire phonon spectrum of the crystal. Such an approach is based on the ab initio framework provided by density functional theory and the construction of a tight-binding effective model via Wannier transformation. The final Hamiltonian includes coupling of the electrons to the crystals phonons, which are also calculated from density functional theory. We apply this methodology to the case of durene, a small π -conjugated molecule, which forms a high-mobility herringbone-stacked crystal. We show that accounting correctly for dispersive forces is fundamental for obtaining a high-quality phonon spectrum, in agreement with experiments. Then, the mobility as a function of temperature is calculated along different crystallographic directions and the phonons most responsible for the scattering are identified.



In the past decade there has been a growing effort aimed at integrating organic materials into electronic devices. In some cases, as for organic field effect transistors¹ or light emitting diodes,² this was motivated by the target of reducing the assembly and processing costs of conventional inorganic devices. In contrast, for some other applications such as flexible displays,³ disposable and wearable electronics,⁴ energy,⁵ spintronics,⁶ and sensors,⁷ organic materials offer properties, which are specific of molecular solids and that cannot be matched by their inorganic counterparts, namely, their mechanical flexibility and the almost unlimited electronic versatility. An analysis of the charge transport of pure molecular crystals is crucial in order to design and improve such applications. Thus, a robust and solid methodology to compute charge transport in molecular crystals is highly desirable.

Theoretical description of charge-carrier transport is often based on the combination between molecular dynamics and kinetic Monte Carlo techniques, which leads to determining the mobility by means of the Einstein relation for diffusive systems.^{8,9} In this case, the coupling of the electrons with lattice dynamics can be modeled by considering a single effective mode¹⁰ to be included in a tight-binding (TB) Hamiltonian or by defining a time-dependent fluctuating transfer integral.⁹ Alternatively, ab initio based approach have been previously performed in the framework of the Holstein–Peierls model,¹¹ where the TB parameters are obtained from a fit of the electronic band structure and the mobility is obtained via the Kubo formula. In this case, phonons are accounted for by calculating the low energy modes via the rigid-molecule approximation.

The main interaction responsible for the, weak, cohesion in molecular crystals is the van der Waals (vdW) force.

Accounting for this interaction is crucial, since it determines the fine structure of a molecular crystal and its elastic properties. These in turn establish the correct amplitude of the intermolecular charge transfer integrals and hence, at low temperature, the polaronic bandwidth. Furthermore, vdW interaction also determines the crystal phonon spectrum, which is the source of dynamic disorder dominating the mobility at high temperature.¹² A large variety of vdW functionals for density functional theory (DFT) have been proposed in recent years, most of which suffer from system-dependency or from the need of introducing empirical parameters.¹³ As such, it is crucial that different vdW-DFT functionals and different numerical implementations are carefully inspected before quantitative results are provided.

In this paper, we present a rigorous methodology, entirely based on DFT, to construct an effective Hamiltonian for the evaluation of the charge-carrier mobility in pure organic crystals, and apply the same to the case of durene (1,2,4,5-tetramethylbenzene). Most of the effort is devoted to the correct estimation of the TB parameters extracted from the ab initio calculations. The most natural way to build a material-dependent Hamiltonian is to project it onto the basis set of its own molecular orbitals. To this end, we calculate the maximally localized Wannier functions¹⁴ (MLWFs) of the crystal, which provide the most straightforward representation of the molecular orbitals and allow us to populate a TB Hamiltonian without any fitting or explicit projection procedure. This, however, is done only after having carefully looked into the effects that different DFT-vdW functionals and implementa-

Received: May 5, 2014

Published: August 28, 2014

tions have on the structural and vibrational properties of the crystal. We have chosen durene as test system because the crystal has a sufficiently small unit cell to be computationally accessible, yet it presents interesting vibrational properties. In fact, its vibrational spectrum presents a low-frequency region attributed to rotations and bendings of the methyl groups and large vibrational amplitudes.¹⁵ Furthermore, durene represents a good reference system since its electronic, vibrational, and conductive properties have been studied experimentally in past years.

1. MODEL

In the following, we describe the theoretical framework used for the computation of the charge mobility. A general Hamiltonian describing charge transport in molecular crystals in the presence of phonons reads as follows

$$H = \sum_{mn} \varepsilon_{mn} a_m^\dagger a_n + \sum_{\lambda} \hbar \omega_{\lambda} \left(b_{\lambda}^\dagger b_{\lambda} + \frac{1}{2} \right) + \sum_{mn\lambda} \hbar \omega_{\lambda} g_{mn}^{\lambda} (b_{\lambda}^\dagger + b_{\lambda}) a_m^\dagger a_n \quad (1)$$

Here, $a_m (a_m^\dagger)$ and $b_{\lambda} (b_{\lambda}^\dagger)$ represent respectively the annihilation (creation) operators for an electron located at the molecule m and for the λ -th phonon mode of frequency ω_{λ} (\hbar is the Heisenberg constant). In the present form, eq 1 includes only the contribution of the phonons at the Γ point. However, it can be generalized to include phonon dispersion by substituting the index λ with $\mathbf{Q} = (\lambda, \mathbf{q})$, where \mathbf{q} is the phonon wavevector. When $n = m$, ε_{mn} describes the on-site energy of the m -th molecule (i.e., of the relevant molecular orbital); in contrast for $m \neq n$, ε_{mn} is the transfer integral between the m -th and n -th molecule. Thus, the first term in the Hamiltonian is simply a tight-binding description of the molecular crystal. The second term describes the phonon energy, while the last one the electron–phonon interaction. The dimensionless quantity g_{mn}^{λ} is the electron–phonon coupling constant for the mode λ , which takes into account both Holstein ($m = n$) and Peierls ($m \neq n$) contributions.

Although all the parameters of eq 1 can be calculated from first-principles, the Hamiltonian remains many-body in nature and there is no exact way for evaluating the associated mobility. In a recent work Bobbert and collaborators^{11,16,17} introduced a canonical transformation for H and then performed thermal averages over the resulting polaron–phonon operators. By using linear-response Kubo formula the charge mobility tensor can be then expressed as

$$\mu_{\alpha\beta}(T) = \frac{e_0}{2k_B T \hbar^2} \sum_{mn} (R_{\alpha m} - R_{\alpha n})(R_{\beta m} - R_{\beta n}) \times \int_{-\infty}^{+\infty} dt e^{-\sum_{\lambda} 2G_{\lambda}[1+2N_{\lambda}-\Phi_{\lambda}(t)] - \Gamma^2 t^2} \times \left[(\varepsilon_{mn} - \Delta_{mn})^2 + \frac{1}{2} \sum_{\lambda} (\hbar \omega_{\lambda} g_{mn}^{\lambda})^2 \Phi_{\lambda}(t) \right] \quad (2)$$

where $R_{\alpha m}$ is the α -th coordinate of site m ,

$$G_{\lambda} = (g_{mm}^{\lambda})^2 + \sum_{k \neq m} (g_{mk}^{\lambda})^2 \quad (3)$$

is the effective electron–phonon coupling constant (there is no explicit dependence on m since the relevant orbitals are equivalent in this case),

$$N_{\lambda} = \frac{1}{e^{\hbar \omega_{\lambda}/k_B T} - 1} \quad (4)$$

is the phonon occupation number for the λ -th mode (k_B is the Boltzmann constant),

$$\Phi_{\lambda}(t) = (1 + N_{\lambda})e^{-i\omega_{\lambda}t} + N_{\lambda}e^{i\omega_{\lambda}t} \quad (5)$$

is the incoherent scattering factor, and finally,

$$\Delta_{mn} = \sum_{\lambda} \hbar \omega_{\lambda} \left[g_{mn}^{\lambda} (g_{mm}^{\lambda} + g_{nn}^{\lambda}) + \frac{1}{2} \sum_{k \neq m,n} (g_{mk}^{\lambda} g_{kn}^{\lambda}) \right] \quad (6)$$

In eq 2 the exponential term, $e^{-\sum_{\lambda} G_{\lambda}(1+2N_{\lambda})}$, describes the polaronic reduction of the transfer integrals with increasing temperature, that is, the temperature-dependent bands narrowing due to the phonons. Such negative exponent leads to a reduction of the mobility as a function of temperature (the temperature dependence is through the phonons' populations). In contrast, the exponential factor containing $\Phi_{\lambda}(t)$ describes incoherent scattering events associated with the emission and adsorption of phonons. This term is also temperature-dependent through the phonons' populations. The sign of the exponent in this case is negative, and the two terms combined determine the slope of the mobility with temperature. Finally, the phenomenological parameter Γ accounts for static disorder and introduces the polarons finite lifetime. In the present work, this is set to a line broadening of $\hbar\Gamma = 0.1$ meV, which represents a well-accepted value for ultrapure crystals.¹¹

2. METHODS

Our calculations have been performed by DFT as implemented in FHI-AIMS¹⁸ and Quantum ESPRESSO.¹⁹ FHI-AIMS is an all-electron code, which was used for obtaining accurate geometries by means of vdW functionals not available elsewhere. In contrast, Quantum ESPRESSO, a pseudopotential implementation of DFT, was employed at the crystal geometries provided by FHI-AIMS as the electronic structure interface to be used with the postprocessing scheme for computing the Wannier functions.

In more detail, the electronic and vibrational properties of durene crystals have been calculated with FHI-AIMS, with the exchange-correlation energy being described by the Perdew–Burke–Ernzerhof (PBE) generalized gradient approximation (GGA).²⁰ Long-range van der Waals interactions have been taken into account with the Tkatchenko and Scheffler (TS) scheme.²¹ The reciprocal space integration was performed over a $(4 \times 4 \times 4)$ Monkhorst–Pack grid.²² A preconstructed high-accuracy all-electron basis set of numerical atomic orbitals was employed, as provided by the FHI-AIMS “tight” default option. Structure optimization was performed with the Broyden–Fletcher–Goldfarb–Shanno algorithm,²³ with the crystal geometry determined by optimizing both the internal coordinates and the supercell lattice vectors with a tolerance of 10^{-3} eV/Å. As a further validation, our calculations have been repeated with the pseudopotential code SIESTA²⁴ by using a real-space mesh-cutoff of 500 Ry, a double- ζ polarized basis set and the same \mathbf{k} -space grid. The phonon spectrum at the Γ point is then obtained with FHI-AIMS within the frozen phonon approach. A displacement of 0.001 Å was applied to each atom of the structure along each of the three spatial directions in order to calculate the forces exerted by all the other atoms. Then, the code Phonopy²⁵ was used to compute the vibrational frequencies and the eigenvectors.

The relaxed crystal structure was then input in the calculation of the MLWFs of the system. To this end, the electronic structures of all the geometries obtained in the previous step were calculated self-consistently with the plane-wave pseudopotential code Quantum ESPRESSO. The wave function was expanded up to a kinetic energy cutoff of 50 Ryd to ensure convergence; the effective potential and the charge density up to 500 Ryd. For the k -space integration, a dense ($8 \times 8 \times 8$) Monkhorst–Pack grid was adopted. The MLWFs were then obtained with the post processing tool Wannier90,²⁶ minimizing their spread until the fractional change was less than 10^{-10} .

3. RESULTS

3.1. Structural and Electronic Properties. Durene molecules are derived from benzene upon substitution of four hydrogen atoms with methyl groups, resulting in an overall D_{2h} symmetry. The lattice structure of durene molecular crystals has been well established experimentally by means of X-ray and neutron diffraction analysis^{27,28} and refined by inelastic neutron scattering.²⁹ It consists of a monoclinic unit cell with space group $P2_1/c(C_{2h}^5)$ containing two molecules, each one composed by 24 atoms (see Figure 1). Durene forms a herringbone crystal, in which the molecules are stacked in a fish bone arrangement along the plane formed by the (010) and the (001) unit vectors.

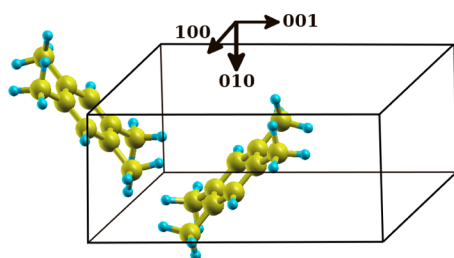


Figure 1. (Color online) Primitive unit cell of a durene molecular crystal. Durene crystallizes in a monoclinic structure with space group $P2_1/c(C_{2h}^5)$. The crystal is characterized by a herringbone arrangement of the molecules along the plane formed by the (010) and the (001) unit vectors. Color code: large yellow spheres, C; small light blue spheres, H.

The cohesive interaction between the molecules in a molecular crystal are of vdW (or dispersive) nature, originating from the attractive interaction between fluctuation-induced dipole moments. Accounting for these interactions within DFT is at present a significant challenge. Standard local and semilocal exchange-correlation functionals, the local density³⁰ and the generalized gradient²⁰ approximations (LDA and GGA), typically fail in reproducing dispersive forces since they lack of any nonlocal contributions to the correlation energy. However, in recent years, several attempts of including dispersive interaction in semilocal functionals have been proposed, and today, one has available a relatively wide range of approximations and implementations of vdW forces in DFT. Among the nonempirical formulations, a large class is occupied by range-separated functionals in which the correlation energy is divided into a short-range local part (treated at the LDA level) and a long-range nonlocal one. These follow the original idea from Langreth and Lundqvist (vdW-DF)^{31–33} and several implementations are now available (for instance see the most recent vdW-DF-C09³⁴). In these, typically, the exchange energy

is described by a GGA as for example the revPBE³⁵ parametrization.

The second class of DFT vdW functionals are based on applying corrections to the DFT energy by summing up the dispersion energies between all the atoms in the system. Typically $C_6 R_{ij}^{-6}$ terms are considered, being R_{ij} the distance between the i -th and the j -th atom, and C_6 the dispersion coefficient. The most common way to introduce such corrections is by defining and estimating empirical parameters, as in the popular Grimme's method.³⁶ More recently, the parameter-free TS scheme has been proposed, where the C_6 coefficients are derived from the electron density of the system and accurate reference data for the free atoms obtained with quantum chemistry methods. In this work, we have tested the performance of different vdW approaches and exchange-correlation functionals in reproducing the experimental structural parameters of durene crystals. For some functional, we have also cross-checked different DFT implementations based on either localized orbital or plane-wave basis sets. For all the functionals we have also benchmarked the geometry of durene in the gas-phase and verified that the differences in the internal molecular coordinates are negligible. These are all within 2% from the experimental data (results not shown here).

In Figure 2, we present the relative deviations $\delta l = (l_{\text{exp}} - l_{\text{calc}})/l_{\text{exp}}$ of the calculated unit cell constants, l_{calc} , from the

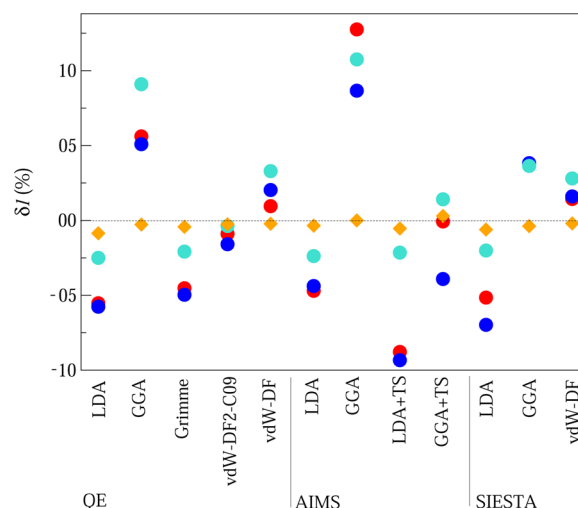


Figure 2. (Color online) Relative deviation of the calculated durene unit cell constants, l_{calc} , with respect to experimental one,²⁹ l_{exp} : $\delta l = (l_{\text{exp}} - l_{\text{calc}})/l_{\text{exp}}$. Performances of different DFT implementations and different exchange and correlation functionals are presented. Color code: red = (100), blue = (010), cyan = (001) lattice parameters; orange = (100)(001) monoclinic angle.

experimental data, l_{exp} , reported in ref 29. As expected,¹³ we notice that in all cases the LDA underestimates the lattice volume, while the GGA (in all cases PBE) overestimates it. Notably, for the LDA, the trend is similar regardless of the particular implementation (code) used. In contrast, the GGA values obtained with the different codes differ in magnitude, probably because the different types of basis sets achieve a different accuracy in evaluating the charge density gradient. In any case, when vdW corrections are not included the deviations are up to 10%, that is, the structure of the molecular crystal is not properly described. The situation, however, improves

drastically when dispersion forces are introduced and the typical δl gets halved.

Going into more detail of the various vdW-DFT flavors, we notice that in general vdW-DFT functionals slightly overestimate the lattice parameters, probably due to their GGA component. An exception is offered by vdW-DF-C09, which in turn shows an agreement with experiments within less than 2% for all the structural quantities investigated. The performance of the TS functional instead depends on the type of local functional it is associated with. Namely, TS performs particularly badly when combined with LDA, while the GGA version leads to a dramatic improvement. While generally the angle of the monoclinic cell is carefully reproduced by all methods, we observe that the largest correction produced by vdW interaction is for the lattice parameter along the (100) direction, the one directed normally to the herringbone plane. This result should not surprise since durenene molecules have little overlap along (100) and their mutual interaction is purely dispersive. In what follows, we decide to adopt the TS-PBE functional for all the calculations, as it combines a good accuracy with a moderate computational cost. The lattice constants are therefore optimized to 6.812 Å 5.360 and 11.660 Å respectively for the (100), (010) and (001) directions, while the angle $(100)(001)$ is 113.0°.

The bandstructure of organic molecular crystals is typically characterized by narrow well-separated manifolds, whose amplitude generally indicates how effective is the charge transfer along the corresponding crystallographic directions. In Figure 3a, we report the bandstructure of the durenene crystal along the high symmetry points of the Brillouin zone, which is depicted in Figure 3b. Since we are interested here in evaluating the hole mobility, we focus our analysis on the valence bands.

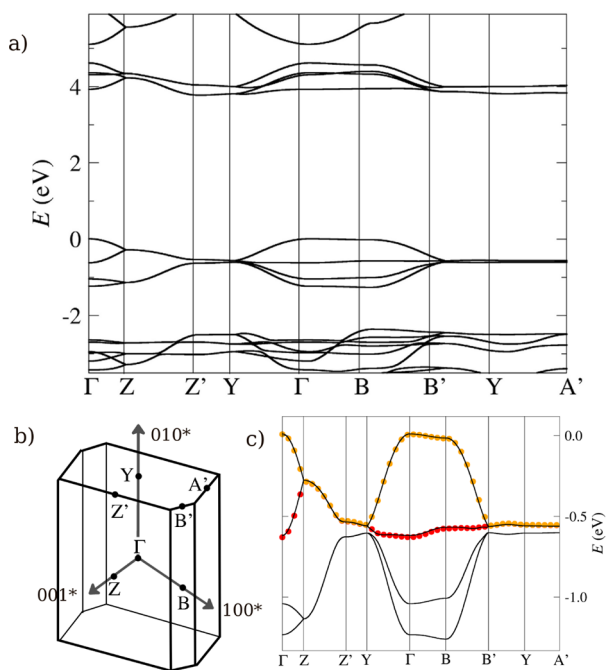


Figure 3. (Color online) Electronic structure of the durenene molecular crystal: (a) bandstructure along the high symmetry points ($E = 0$ is the top of the valence band); (b) Brillouin zone of the durenene crystal, space group $P2_1/c(C_{2h}^2)$; (c) zoom of the HOMO and HOMO-1 related bands as obtained from DFT (solid line) and from the Wannier functions (dots).

Two manifolds appear below $E = E_F = 0$ eV (E_F is the Fermi level), whose energy region has been magnified in Figure 3c. An analysis of the local density of states shows that the two bands belonging to the upper manifold (i.e., those ranging from 0.0 and -0.6 eV at Γ) derive from the high occupied molecular orbital (HOMO) of the two molecules in the unit cell. Similarly, the lower bands located between -1.0 and -1.2 eV at Γ , originate from the HOMO-1 orbitals. The HOMO bandwidth is only 0.68 eV, and it is due to the interaction of the two molecules within the unit cell. This value is larger than that of other popular high-mobility organic crystals such as rubrene (~ 0.4 eV)³⁷ or oligoacenes (~ 0.1 – 0.5 eV),³⁸ suggesting potentially good charge transport properties.

The bandstructure also provides hints on the anisotropy of the charge mobility. In the valence band, in fact, we notice the presence of regions with almost flat dispersion, $\overline{\Gamma B}$ and $\overline{YA'}$, which correspond to directions orthogonal to the herringbone plane. This is an indication of poor mobility along those directions. On the contrary, the finite dispersion of the bands in other regions [$\overline{\Gamma Z}$ corresponding to (001) and $\overline{\Gamma Y}$ corresponding to (010)] indicates more effective in-plane charge transport. It is well-known that standard exchange and correlation functionals underestimate the electronic bandgap, while this issue is partially recovered by hybrid functionals. A calculation of the bandstructure with the B3LYP³⁹ hybrid functional reveals that the gap enlarges from 4.7 to 5.4 eV, yet the structure and the bandwidth of the valence band manifolds remain essentially unaltered, at least for those bands close to E_F . This allows us to analyze the hole mobility by relying on the PBE bandstructure.

3.2. Vibrational Properties. Phonons in molecular crystals are quantized harmonic displacements of the atoms forming the molecules from their equilibrium positions. Unlike the case of conventional atomic crystals, in molecular crystals there appear both intramolecular and intermolecular modes. The first are internal vibrations of the individual molecules, while the second are associated with rigid displacements of the molecules in the crystal with respect of each other. Since the durenene crystal contains two 24-atom molecules in the unit cell, it can sustain 12 intermolecular modes and 129 intramolecular ones. A careful description of the low-energy modes is essential to correctly simulate charge transport in such systems. In many cases one uses the rigid-molecule approximation, in which only intermolecular modes are considered and the molecules are treated as rigid units. While this approximation might be reasonable for planar molecules such as oligoacenes, it is not for the case of durenene because of the high flexibility of the methyl groups. In fact, our calculated displacement patterns show that the higher intermolecular modes are always accompanied by a rotation/flexing of the methyl groups interacting among neighboring molecules, thus effectively constituting hybrid modes.

In Figure 4, we compare the phonon density of states (pDOS) at the Γ point calculated with and without the inclusion of vdW interactions, and divide the spectrum into 5 regions according to the nature of the phonons. The first vertical line separates the intermolecular modes (region I) from the intramolecular ones (regions II–V). Let us start our analysis from the intramolecular vibrations. The region II is characterized by torsional and stretching vibrations of the methyl-C bonds. Here, the left peaks originate from pure movements of the methyl groups, while the structure on the right involves also rigid motions of the C_6 ring. Then, in region

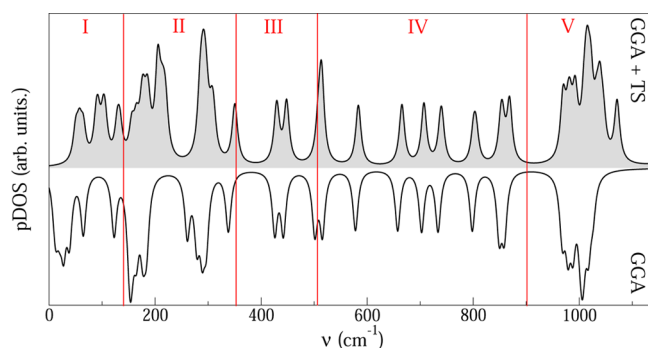


Figure 4. Phonon density of states (pDOS), where the results for GGA (upper curve) are compared to those obtained with GGA+TS (lower curve). The vertical lines mark the boundaries between regions characterized by similar vibrations.

III, the modes are attributed to distortions of the C_6 ring, while around 500 cm^{-1} stretching of the molecules along their symmetry axes gives rise to a high peak. At higher frequencies, region IV, we first observe mixed C_6 and methyl-C modes, and finally, the large structure in region V involves C–H vibrations. As expected from the fact that intramolecular vibrations concern mainly covalent bonds, we do not appreciate any notable differences between the GGA and the GGA+TS (including vdW interaction) spectra, which both remain essentially similar to that of the molecule in the gas phase. On the contrary, major differences arise in the intermolecular region I, where the effect of the vdW interactions is that of reducing the intermolecular distances leading to a reduction of the crystal “softness”. As a consequence the intermolecular modes calculated when considering vdW forces blue-shift with respect to their GGA values.

In Figure 5, we compare our GGA+TS-calculated vibrational spectra with experimental data obtained with inelastic neutron scattering (INS), infrared spectroscopy (IR), and Raman spectroscopy. Because of the various selection rules each of these techniques captures a different portion of the vibrational

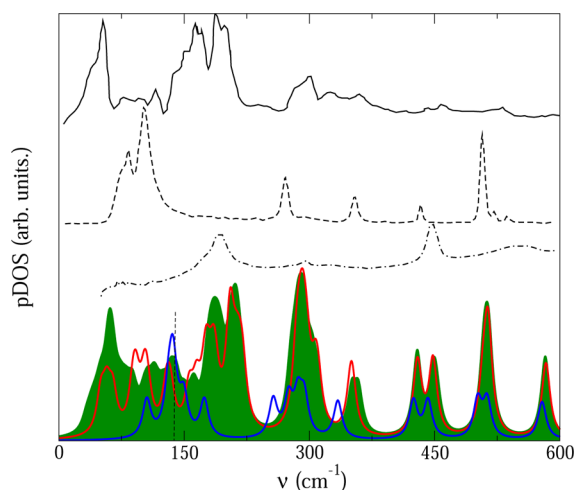


Figure 5. (Color online) Phonon density of states (pDOS) of the durene crystal. The upper three curves refer to the INS (solid), Raman (dashed), IR (dash-dotted) experimental data as extracted from ref 15. The lower curves are the calculated data for durene in the gas phase (blue) and for the single crystal described by using either a $1 \times 1 \times 1$ (red) or a $2 \times 2 \times 2$ (green) supercell.

spectrum. Note that no selection rules are applied when plotting our calculated pDOS, which then provides information only on the energy positions of the vibrational excitations, but not on their intensity. In the figure, we present calculations for the molecule in the gas phase and for the durene crystal described by either the unit cell or a $2 \times 2 \times 2$ supercell. This larger cell allows us to capture additional modes with wavelength longer than those accessible in the unit cell. In particular the $2 \times 2 \times 2$ supercell partially includes optical phonons, which account for out-of-phase vibrations between molecules in neighboring unit cells. As such, the $2 \times 2 \times 2$ supercell returns a pDOS with a spectral amplitude in the intermolecular region, namely, for frequencies smaller than $\sim 200\text{ cm}^{-1}$, significantly larger than that of the unit cell. This overall improves the calculated spectrum, which is now in better agreement with the experiments as measured by INS.¹⁵ At higher frequencies the three calculated spectra are rather similar and nicely reproduce the peaks present in either the experimental infrared or the Raman spectrum. Interestingly, we also notice a few regions in the intermolecular part of the spectrum where the calculated modes for the gas phase overlap with those obtained for the crystal. This is the range where hybrid inter/intramolecular modes appear. In conclusion, we find that the GGA+TS exchange and correlation functional provides an accurate description of the phonon spectrum of durene crystals, and this will be then used for evaluating the mobility.

3.3. Construction of an Effective Tight-Binding Model.

The next task in the process of evaluating the mobility of durene crystals is that of extracting the TB parameters appearing in eq 1 from our accurate DFT calculations. In general there are several strategies to achieve such goal. For instance, one can use the “dimer method”, which consists in calculating the transfer integrals as matrix elements of the Fock operator with respect to the relevant orbitals in a molecular dimer.^{40,41} Other methods rely on fitting the bandstructure to a model dispersion function containing several parameters.^{42,43} In this work, we extract the TB parameters by the rigorous calculation of the MLWFs of the system. Such scheme does not involve band fitting, and it is particularly suitable for the bandstructure of durene, since both the conduction and the valence band are well separated by the rest of the manifold. In our case, we are interested in the hole mobility, and therefore, we have constructed the MLWFs only for the uppermost valence manifold.

The calculated MLWFs for the uppermost valence band are depicted in Figure 6. These orbitals (two per unit cell, one on each molecule) are essentially identical to the HOMO of the durene molecule in the gas phase, as expected from the fact that the intermolecular interaction is relatively weak (the valence bandwidth is less than 1 eV). The bandstructure associated with such MLWFs perfectly reproduces that calculated from DFT, as demonstrated in Figure 3, so that our MLWFs’ representation of the bandstructure is accurate and at the same time returns the clear physical interpretation of the valence band as the HOMO-derived one.

In Table 1 we report the most relevant (largest) TB parameters, which are also visualized in Figure 7. The on-site energy, $\epsilon_{11}(000)$, is the same for the two MLWFs of the two molecules in the unit cell, being them equivalent in the lattice. Note that here we have used the notation $\epsilon_{nm}(abc)$, where the indices n and m label the molecule in the cell ($n, m = 1, 2$), while the vector (a, b, c) is a generic direct lattice vector written

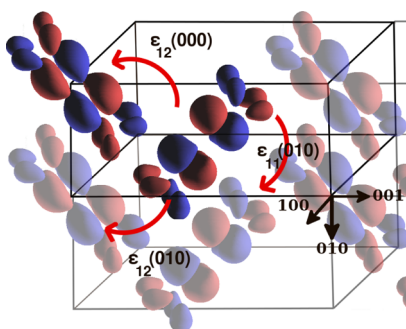


Figure 6. (Color online) Real-space representation of the MLWFs constructed from the two uppermost valence bands of the durene crystal.

Table 1. Dominant TB Parameters for the Durene Crystal^a

| transfer integral | energy (meV) |
|---|--------------|
| $\epsilon_{11}(000) = \epsilon_{22}(000)$ | 574 |
| $\epsilon_{12}(000) = \epsilon_{12}(010)$ | 73 |
| $\epsilon_{11}(010)$ | 63 |
| $\epsilon_{11}(001)$ | 2 |
| $\epsilon_{11}(100)$ | 0.8 |
| $\epsilon_{12}(100)$ | 4 |
| $\epsilon_{11}(011)$ | 3 |
| $\epsilon_{12}(011)$ | 73 |

^aThe indexes identify the molecule in the unit cell, while the brackets contain the components of a generic direct lattice vector written in terms of the crystal unit lattice vectors.

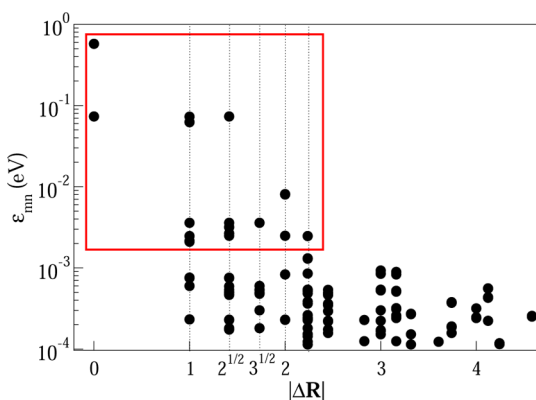


Figure 7. Absolute value of the calculated transfer integrals as obtained from the MLWFs of the durene crystal. $\Delta\mathbf{R}$ is the real-space lattice position expressed in terms of the lattice vectors components. The matrix elements included in the calculation of the mobility are those enclosed by the box.

in terms of the crystal unit lattice vectors. The transfer integrals for the in-plane neighboring molecules are $\epsilon_{12}(000)$ [which is equivalent to $\epsilon_{12}(010)$] and $\epsilon_{11}(010)$. Their values are close to each other and an order of magnitude larger than those between molecules located on different herringbone planes. Accordingly, it is reasonable to expect the out-of-plane mobility to be at least 1 order of magnitude smaller than the in-plane one, as already deduced from the bandstructure analysis.

The absolute values of all the calculated transfer integrals are shown in Figure 7. These are plotted against the real-space lattice position $\Delta\mathbf{R}$, expressed in terms of the lattice vectors components. As such $\Delta\mathbf{R} = 0$ indicates matrix elements between MLWFs placed in the same cell, $\Delta\mathbf{R} = 1$ is for matrix

elements between orbitals in nearest neighboring cells, etc. Apart from the largest matrix element for $\Delta\mathbf{R} = 0$, which represents the on-site energy, the most dominant transfer integrals have the same magnitude whether connecting molecules located along the in-plane neighboring cells or along the in-plane diagonal cells. Notably, the transfer integrals decay rather rapidly as the distance between the molecules increases. As such, we have decided to retain for the calculation of the mobility only those, which fall in the red box of Figure 7. These are at least 1 order of magnitude larger than those been excluded and alone provide an excellent description of the bandstructure.

In order to obtain the electron–phonon coupling matrix elements, g_{mn}^{λ} , we adopt the following procedure. Having selected a particular phonon mode, λ , we apply to each atom i in the unit cell a displacement, $Q_{\lambda} \cdot \mathbf{e}_i^{\lambda}$, along the corresponding phonon eigenvector \mathbf{e}_i^{λ} , where Q_{λ} is a scalar determining the amplitude of the displacement. We then repeat the calculation of the MLWFs for this new geometry, thus obtaining a new set of Hamiltonian parameters, ϵ_{mn} . Then the electron–phonon coupling can be computed by numerical differentiation as $g_{mn}^{\lambda} = (1/(\omega_{\lambda}(\hbar\omega_{\lambda})^{1/2}))(\partial\epsilon_{mn}/\partial Q_{\lambda})$. We have carefully tested the choice of Q_{λ} , by looking at the variation of some relevant matrix elements as a function of Q_{λ} , ranging from 0.01 to 1 (the displacement vectors, \mathbf{e}_i^{λ} , are normalized). This is a rather delicate exercise. If Q_{λ} is too small, numerical errors will be dominant, but if Q_{λ} is large the harmonic approximation will break down. From our analysis, we have concluded that $Q_{\lambda} = 0.10$ is a reasonable choice.

We have then analyzed the phonon eigenvectors and selected 30 modes to be included in the mobility calculation. These comprise all the intermolecular modes and all the symmetry-inequivalent intramolecular distortions in the energy range 0–550 cm^{-1} . Phonon modes of much higher energy are not excited at experimentally accessible temperatures. For all the selected modes, we have calculated the electron–phonon coupling constants, g_{mn}^{λ} and the effective coupling parameters, G_{λ} [see eq 3]. These are shown in Figure 8. Note that the quantity G_{λ} includes information about both the local (Holstein) and nonlocal (Peierls) electron–phonon couplings for a given mode λ and therefore it provides an estimate of how strongly a given mode affects the electronic properties of the system.

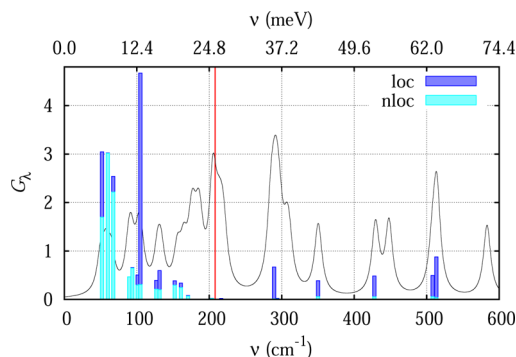


Figure 8. (Color online) Effective electron–phonon couplings, G_{λ} , (histogram) and pDOS (solid line). For each frequency, the relative intensity of the local (Holstein) and nonlocal (Peierls) contribution is shown in cyan and blue, respectively. The room-temperature thermal energy is highlighted by a vertical red line. Phonon energies are reported both in eV (upper scale) and cm^{-1} (lower scale).

By inspecting Figure 8, we notice that the prominent G_λ values are the ones related to the intermolecular modes, namely, those with energy below 17 meV. In particular, the first three modes involve rotations along the molecular z axes and translation along the (100) crystallographic direction. The mode with large G_λ appearing at 13 meV corresponds to molecular rotations along their relative C_2 axis. For energies lower than the room-temperature thermal energy there is an additional handful of modes, which contribute, even though with a lower impact, to the mobility. These are low-energy intermolecular vibrations of the C-methyl bonds, which produce a redistribution of the charge density, which in turn affects the magnitude of the transfer integrals. We finally notice the presence of few high-frequency modes with large G_λ , which may play a role in the transport, especially at high temperature. It is worth mentioning that the nonlocal contribution to G_λ is significant only in the lower part of the spectrum, while for large frequencies the nature of the G_λ is essentially local.

3.4. Mobility. We are now in the position to evaluate the temperature-dependent hole mobility of the durene crystal by using the linear approximation of eq 2. Our results are presented in Figure 9, where we show the hole mobility along

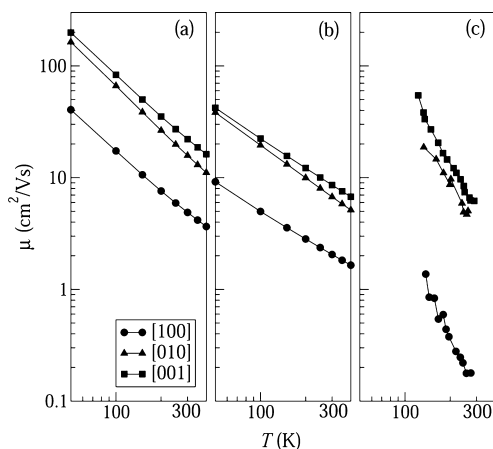


Figure 9. Durene hole mobilities as a function of temperature calculated by including (a) only intermolecular modes, (b) both inter- and intramolecular modes, together with (c) the experimental data of ref 44. The mobility is calculated/measured along the following directions: (100), circles; (010), triangles; and (001), squares.

three different crystallographic directions and calculated either by including all the selected inter- and intramolecular modes (Figure 9b) or by considering only the intermolecular ones (Figure 9a). Calculations are compared with the experimental data from ref 44.

As already pointed out in the past⁴⁵ the temperature dependence of the durene mobility, μ , can be associated with band-like transport, as μ decreases with increasing temperature. A second notable feature is that the anisotropy of the transfer integrals arising from the bandstructure reflects in the transport properties. In fact, the mobility along the (100) direction is an order of magnitude smaller than that in-plane. These two facts are in agreement with the experimental data. Interestingly, when one moves from considering only intermolecular modes to the entire phonon spectrum, two main effects arise. First there is a renormalization of the mobility intensity, namely, a shift of the entire $\mu(T)$ curve toward lower mobility values. The shift is such that μ calculated by including the entire phonon

spectrum matches rather well the experimental one (along the in-plane directions) at room temperature. This suggests that including the entire phonon spectrum, or at least those modes relevant in the temperature range up to room temperature, is fundamental to describe the high-temperature limit of the mobility of durene.

The second effect is that the progressive inclusion of modes causes a variation of the temperature dependence of the mobility, which in general follows a power law, T^γ . While for the case of panel (a) we have $\gamma = -1.2$, for (b) this changes to -0.9 , and these values have to be compared with the experimentally determined γ , which ranges between -2.1 and -2.8 . Given such a large mismatch between theory and experiments over the exponents γ , we have estimated the robustness of our results with respect to variations of the computed Hamiltonian parameters. In Figure 10 we illustrate

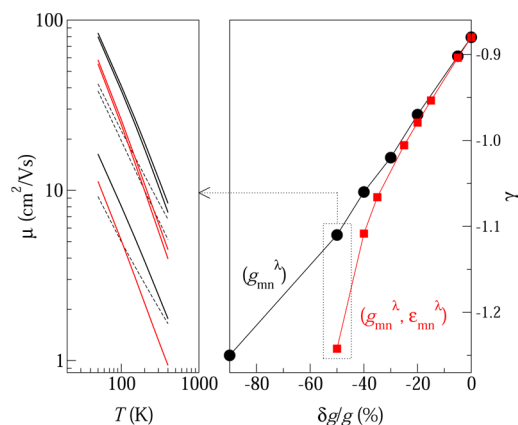


Figure 10. (Color online) Sensitivity of the calculated mobility to the tight-binding parameters. In the right panel, we show the exponent γ describing the power-law dependence of μ over T as a function of the relative reduction of the tight-binding parameters, $\delta g/g$. In particular, we consider rescaling g_{mn}^λ only (black) and both g_{mn}^λ and ϵ_{mn} (red). The actual mobility as a function of the temperature is plotted in the right panel for the two cases corresponding to a 50% percent relative reduction of the parameters (same color order) and for the unaltered case (dashed lines).

how the temperature dependence of the mobility varies as a function of the relative reduction of g_{mn}^λ only and of both g_{mn}^λ and ϵ_{mn} . The main message from this analysis is that in both cases even an alteration of the parameters as drastic as 50% leads to a reduction of γ of only 20–30%. This means that the difference between the experimental temperature dependence of the mobility and the one calculated here cannot be ascribed to a potential inaccuracy in the determination of the tight-binding parameters.

The mismatch between the computed and the experimental γ can be ascribed to the level of theory adopted in this work, which although being able to describe both the high and the low temperature limit, still assumes a polaronic nature of the charge carriers. In particular, the approximations leading to our eq 2 bring two main consequences. On the one hand, dynamic disorder is not fully included, since the temperature dependence of the mobility is only through a renormalization of the energy bands driven by thermal averages. As such, the theory is expected to be problematic when the role of dynamic disorder is enhanced, as in the case of small molecules with large interactions in the crystal structure (i.e., as in the case of durene). On the other hand, a second and minor issue is related

to the fact that the finite lifetime of polarons due to disorder enters in eq 2 through an adjustable parameter Γ . In this work, Γ is assumed to be constant with temperature and identical for each crystalline directions, a clear simplification of the actual experimental situation.

Yet, the theory presented here can still describe changes in the slope of the mobility as a function of temperature. In Figure 11 we present an expanded $\mu(T)$ plot where we extend the

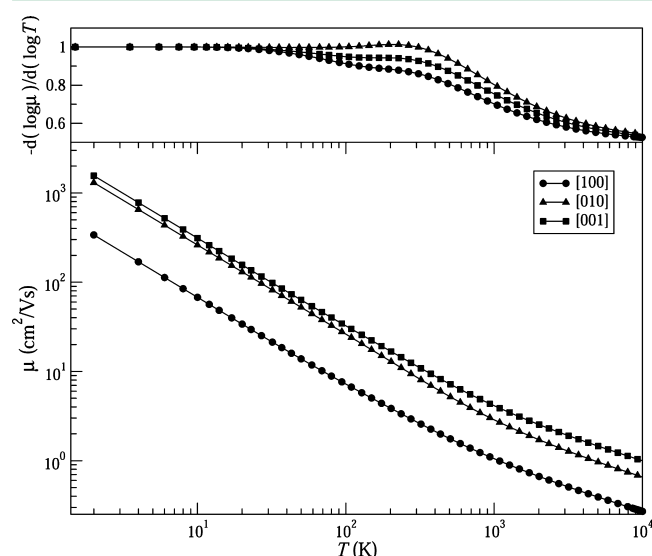


Figure 11. Durene hole mobilities as a function of temperature calculated by including both inter- and intramolecular modes over a large temperature range. The mobility is calculated for the following directions: (100), circles; (010), triangles; and (001), squares. The upper panel presents the same data with μ plotted on a logarithmic scale.

temperature range to 10^4 K. Clearly one can notice a change of slope in the temperature dependence of the mobility as we approach temperatures larger than 300 K. As mentioned before, this is driven by the interplay between the bands-narrowing and the incoherent scattering term in eq 2, which are both temperature dependent. Note that the change in slope occurs at a typical temperature significantly smaller than the bandwidth, that is, in a situation where the band-transport picture should hold well. To the best of our knowledge, such a change in slope has never been measured experimentally for durene; however, we have not been able to find measurements of mobility for temperatures beyond room temperature. As such our prediction remains open to a future experimental validation.

4. CONCLUSIONS

In conclusion, we have presented a rigorous method for constituting an effective Hamiltonian for the evaluation of the mobility of a molecular crystal as a function of temperature and it has been applied to the case of durene single crystals. Our computational scheme proceeds first with an accurate evaluation of both the structural and vibrational properties of the crystal as obtained with DFT including van der Waals interaction. Then, an effective tight-binding model incorporating also electron–phonon coupling is constructed via the rigorous calculation of the MLWFs reproducing the DFT-calculated band structure. This step does not rely on a fitting procedure and allows us to evaluate the various hopping parameters up to an arbitrary number of neighbors. Finally, the

mobility is computed by using a mean-field-like expression based on linear response Kubo's formula.

We found several points of agreement with the experimental data. A careful test of the vdW approach allows for an excellent description of the structure and of the phonons. As for the mobility calculations, our approach reproduces the experimental bandlike behavior, the anisotropy and reasonably the spanned range. Yet we found some disagreement on the mobility scaling with temperature.

Our findings suggest that intermolecular phonons contribute the most to determining the mobility, but the inclusion of the entire low-energy spectrum is necessary to reproduce the experimentally measured room-temperature value. Unfortunately the theory is not capable of describing the experimentally measured exponent of the power law relating mobility and temperature. This is due to the mean field nature of our calculated mobility, in which the effect of the temperature enters only as a renormalization of the electronic bands, but dynamical disorder is not taken into account. Given this analysis, our procedure can be refined by including a higher level of description to the final determination of the mobility.

AUTHOR INFORMATION

Corresponding Author

*Email: carlomotta84@gmail.com.

Notes

The authors declare no competing financial interest.

ACKNOWLEDGMENTS

This work is sponsored by the European Research Council (QUEST project). Computational resources have been provided by the supercomputer facilities at the Trinity Center for High Performance Computing and at ICHEC (project tcopy038b).

REFERENCES

- (1) Yan, H.; Chen, Z.; Zheng, Y.; Newman, C.; Quinn, J. R.; Dotz, F.; Kastler, M.; Facchetti, A. *Nature* **2009**, *457*, 679–687.
- (2) Tang, W.; Vanslyke, S. A. *Appl. Phys. Lett.* **1987**, *51*, 913–915.
- (3) Wong, W.; Salleo, A. *Flexible Electronics: Materials and Applications*; Springer: New York, 2009.
- (4) Forrest, S. R. *Nature* **2004**, *428*, 911–918.
- (5) Thompson, B.; Fréchet, J. *Angew. Chem., Int. Ed.* **2008**, *47*, 58–77.
- (6) Sanvito, S. *Chem. Soc. Rev.* **2011**, *40*, 3336–3355.
- (7) Torsi, L.; Dodabalapur, A. *Anal. Chem.* **2005**, *77*, 380A–387 A.
- (8) Rühle, V.; Lukyanov, A.; May, F.; Schrader, M.; Vehoff, T.; Kirkpatrick, J.; Baumeier, B.; Andrienko, D. *J. Chem. Theor. Comp.* **2011**, *7*, 3335–3345.
- (9) Wang, L.; Li, Q.; Shuai, Z.; Chen, L.; Shi, Q. *Phys. Chem. Chem. Phys.* **2010**, *12*, 3309–3314.
- (10) Troisi, A. *Adv. Mater.* **2007**, *19*, 2000–2004.
- (11) Hannewald, K.; Bobbert, P. A. *Appl. Phys. Lett.* **2004**, *85*, 1535–1537.
- (12) Troisi, A.; Orlandi, G. *Phys. Rev. Lett.* **2006**, *96*, 086601.
- (13) Tkatchenko, A.; Romaner, L.; Hofmann, O. T.; Zojer, E.; Ambrosch-Draxl, C.; Schefer, M. *MRS Bull.* **2010**, *35*, 435–442.
- (14) Marzari, N.; Mostofi, A. A.; Yates, J. R.; Souza, I.; Vanderbilt, D. *Rev. Mod. Phys.* **2012**, *84*, 1419–1475.
- (15) Pawlućojć, A.; Natkaniec, I.; Bator, G.; Sobczyk, L.; Grech, E.; Nowicka-Scheibe, J. *Spectrosc. Acta Part A* **2006**, *63*, 766–773.
- (16) Hannewald, K.; Stojanović, V. M.; Schellekens, J. M. T.; Bobbert, P. A.; Kresse, G.; Hafner, J. *Phys. Rev. B* **2004**, *69*, 075211.
- (17) Hannewald, K.; Bobbert, P. A. *Phys. Rev. B* **2004**, *69*, 075212.

- (18) Blum, V.; Gehrke, R.; Hanke, F.; Havu, P.; Havu, V.; Ren, X.; Reuter, K.; Scheffler, M. *Comput. Phys. Commun.* **2009**, *180*, 2175–2196.
- (19) Giannozzi, P.; Baroni, S.; Bonini, N.; Calandra, M.; Car, R.; Cavazzoni, C.; Ceresoli, D.; Chiarotti, G. L.; Cococcioni, M.; et al. *J. Phys.: Condens. Matter* **2009**, *21*, 395502.
- (20) Perdew, J. P.; Burke, K.; Ernzerhof, M. *Phys. Rev. Lett.* **1996**, *77*, 3865–3868.
- (21) Tkatchenko, A.; Scheffler, M. *Phys. Rev. Lett.* **2009**, *102*, 073005.
- (22) Monkhorst, H. J.; Pack, J. D. *Phys. Rev. B* **1976**, *13*, 5188–5192.
- (23) Press, W. H.; Teukolsky, S. A.; Vetterling, W. T.; Flannery, B. P. *Numerical Recipes*, 3rd ed.; Cambridge University Press: Cambridge, U.K., 1997.
- (24) Soler, J. M.; Artacho, E.; Gale, J. D.; García, A.; Junquera, J.; Ordejón, P.; Sánchez-Portal, D. *J. Phys.: Condens. Matter* **2002**, *14*, 2745–2779.
- (25) Togo, A.; Oba, F.; Tanaka, I. *Phys. Rev. B* **2008**, *78*, 134106.
- (26) Mostofi, A. A.; Yates, J. R.; Lee, Y.-S.; Souza, I.; Vanderbilt, D.; Marzari, N. *Comput. Phys. Commun.* **2008**, *178*, 685–699.
- (27) Stam, C. H. *Acta Cryst. B* **1972**, *28*, 2630–2632.
- (28) Prince, E.; Schroeder, L. W.; Rush, J. J. *Acta Cryst. B* **1973**, *29*, 184.
- (29) Plazanet, M.; Johnson, M.; Gale, J.; Yildirim, T.; Kearley, G.; Fernández-Díaz, M.; Sánchez-Portal, D.; Artacho, E.; Soler, J.; Ordejón, P.; García, A.; Trommsdorff, H. *Chem. Phys.* **2000**, *261*, 189–203.
- (30) Ceperley, D. M.; Alder, B. J. *Phys. Rev. Lett.* **1980**, *45*, 566–569.
- (31) Andersson, Y.; Langreth, D. C.; Lundqvist, B. I. *Phys. Rev. Lett.* **1996**, *76*, 102–105.
- (32) Dion, M.; Rydberg, H.; Schröder, E.; Langreth, D. C.; Lundqvist, B. I. *Phys. Rev. Lett.* **2004**, *92*, 246401.
- (33) Langreth, D. C.; Lundqvist, B. I.; Chakarova-Käck, S. D.; Cooper, V. R.; Dion, M.; Hyldgaard, P.; Kelkkanen, A.; Kleis, J.; Kong, L.; S, L.; et al. *J. Phys.: Condens. Matter* **2009**, *21*, 084203.
- (34) Cooper, V. R. *Phys. Rev. B* **2010**, *81*, 161104.
- (35) Zhang, Y.; Yang, W. *Phys. Rev. Lett.* **1998**, *80*, 890–890.
- (36) Grimme, S. *J. Comput. Chem.* **2006**, *27*, 1787.
- (37) Da Silva Filho, D. A.; Kim, E. G.; Brédas, J. L. *Adv. Mater.* **2005**, *17*, 1072–1076.
- (38) Hummer, K.; Ambrosch-Draxl, C. *Phys. Rev. B* **2005**, *72*, 205205.
- (39) Vosko, S. H.; Wilk, L.; Nusair, M. *Can. J. Phys.* **1980**, *58*, 1200–1211.
- (40) Troisi, A.; Orlandi, G. *J. Phys. Chem. A* **2006**, *110*, 4065–4070.
- (41) Akande, A.; Bhattacharya, S.; Cathcart, T.; Sanvito, S. *J. Chem. Phys.* **2014**, *140*, 074301.
- (42) Wang, L. J.; Peng, Q.; Li, Q. K.; Shuai, Z. *J. Chem. Phys.* **2007**, *127*, 044506.
- (43) Ortmann, F.; Bechstedt, F.; Hannebald, K. *Phys. Status Solidi B* **2011**, *248*, 511–525.
- (44) Burshtein, Z.; Williams, D. F. *Phys. Rev. B* **1977**, *15*, 5769–5779.
- (45) Ortmann, F.; Hannebald, K.; Bechstedt, F. *Appl. Phys. Lett.* **2008**, *93*, 222105.